EDGE ARTICLE

The interplay between fluorescence and phosphorescence with luminescent gold(I) and gold(III) complexes bearing heterocyclic arylacetylide ligands†

Kaai Tung Chan,[a] Glenna So Ming Tong,*[a] Wai-Pong To,[a] Chen Yang,[a] Lili Du,[b] David Lee Phillips[b] and Chi-Ming Che*[ac]

The photophysical properties of a series of gold(I) [LAu(C≡CR)] (L = PCy₃ (**1a–4a**), RNC (**5a**), NHC (**6a**)) and gold(III) complexes [Au(C^N^C)(C≡CR)] (**1b–4b**) bearing heterocyclic arylacetylide ligands with narrow band-gap are compared. The luminescence of both series are derived from an intraligand transition localized on the arylacetylide ligand ($\pi\pi^*(C\equiv CR)$) but **1a–3a** displayed prompt fluorescence (τ_{PF} = 2.7–12.0 ns) while **1b–3b** showed mainly phosphorescence (τ_{Ph} = 104–205 μs). The experimentally determined intersystem crossing (ISC) rate constants (k_{ISC}) are on the order of 10^6 to 10^8 s^{-1} for the gold(I) series (**1a–3a**) but 10^{10} to 10^{11} s^{-1} for the gold(III) analogues (**1b–3b**). DFT/TDDFT calculations have been performed to help understand the difference in the k_{ISC} between the two series of complexes. Owing to the different oxidation states of the gold ion, the Au(I) complexes have linear coordination geometry while the Au(III) complexes are square planar. It was found from DFT/TDDFT calculations that due to this difference in coordination geometries, the energy gap between the singlet and triplet excited states (ΔE_{ST}) with effective spin–orbit coupling (SOC) for Au(I) systems is much larger than that for the Au(III) counterparts, thus resulting in the poor ISC efficiency for the former. Time-resolved spectroscopies revealed a minor contribution (<2.9%) of a long-lived delayed fluorescence (DF) (τ_{DF} = 4.6–12.5 μs) to the total fluorescence in **1a–3a**. Attempts have been made to elucidate the mechanism for the origins of the DF: the dependence of the DF intensity with the power of excitation light reveals that triplet–triplet annihilation (TTA) is the most probable mechanism for the DF of **1a** while germinate electron–hole pair (GP) recombination accounts for the DF of **2a** in 77 K glassy solution (MeOH/EtOH = 4 : 1). Both **4a** and **4b** contain a BODIPY moiety at the acetylide ligand and display only ^{1}IL($\pi\pi^*$) fluorescence with negligible phosphorescence being observed. Computational analyses attributed this observation to the lack of low-lying triplet excited states that could have effective SOC with the S$_1$ excited state.

Introduction

Phosphorescence is a distinctive photophysical property of transition-metal complexes, which has widespread applications in diverse areas. As it is derived from the 'forbidden' radiative relaxation of a triplet-excited state to the singlet ground state, it is featured by long emission lifetime (in μs) and reduced emission energy compared to fluorescence commonly encountered in organic luminophores. Electronic transitions associated with a change of spin are prohibited by the spin-selection rule. However, transition-metal ions that have high atomic number and hence, large spin–orbit coupling constant (ξ), usually lead to efficient spin–orbit coupling (SOC) that relaxes the spin selection rule. Fast intersystem crossing (ISC) in the sub-picosecond to picosecond time regime[1] leads to rapid depletion of a singlet excited state to a triplet excited state instead of fluorescence as fluorescence radiative lifetime is typically in the nanosecond range. Thus, in transition-metal complexes, phosphorescence normally prevails in their luminescence spectra.

However, in recent years, there are an increasing number of reports on transition-metal complexes which display slow ISC

[a]State Key Laboratory of Synthetic Chemistry, Institute of Molecular Functional Materials, Department of Chemistry, The University of Hong Kong, Pokfulam Road, Hong Kong SAR, China. E-mail: tongsm@hku.hk; cmche@hku.hk

[b]Department of Chemistry, The University of Hong Kong, Hong Kong, China

[c]Department of Chemistry, HKU Shenzhen Institute of Research and Innovation, Shenzhen 518053, China

rate with lifetimes ranging from hundreds of ps to ns. For instance, 2,5-bis(arylethynyl)rhodacyclopentadiene complexes ($\xi_{Rh} = 1260$ cm^{-1})[2] were reported to display exclusively prompt fluorescence with high emission quantum yields of 0.3–0.7 and lifetimes of 1–3 ns, corresponding to ISC rate constants of $\sim 10^8$ s^{-1}.[3] In addition, transition-metal complexes containing fused aromatic systems such as perylene, perylene diimide, pyrene and tetracene also show ligand-dominated fluorescence (see Fig. 1).[4] Hence, it has become clear that the presence of heavy elements does not guarantee fast ISC rate; the molecular structure and the nature of the ligands may play more critical roles in determining the ISC rate.

Luminescent Au(I) complexes are well documented to display rich photophysical properties. Although Au(I) complexes generally display phosphorescence owing to the large SOC constant of Au(I) ion ($\xi_{Au} \sim 5100$ cm^{-1}),[2] ligand-centered fluorescence has also been reported in a number of gold(I) complexes. For example, as revealed by the luminescence of [TEE(AuPCy$_3$)$_4$] and [TEB(AuPCy$_3$)$_3$] (TEE = tetraethynylethene; TEB = 1,3,5-triethynylbenzene), subtle changes in the electronic structure of the bridging alkynyl ligand leads to intense phosphorescence ($\Phi_{em} = 0.46$, $\tau = 285$ μs) in the latter but solely fluorescence ($\Phi_{em} = 0.22$, $\tau < 0.05$ μs) in the former.[5] In both cases, the luminescence originates from the ligand-centered transition mainly localized on the bridging alkynyl ligands. Che and co-workers also reported a series of Au(I)-conjugated acetylides, [(Cy$_3$P)Au(C≡C–C$_6$H$_4$)$_{n-1}$(C≡CPh)] ($n \geq 2$), which display dual fluorescence (prompt and delayed) and phosphorescence.[6] Both the Φ_{em} and ratio of fluorescence versus phosphorescence were found to depend on the conjugation length (number of repeating units n) and the substitution pattern of arylacetylide ligands.

As a continuous effort to elucidate the ligand effects on the photophysics of luminescent gold complexes, heterocyclic arylacetylide ligands containing narrow band-gap moieties (benzothiadiazole (L1), coumarin (L2), naphthalimide (L3) and boron-dipyrromethene (referred to as Bodipy) (L4); Chart 1) were chosen in this study. A series of Au(I) heterocyclic arylacetylide complexes, 1a–4a, were synthesized. Tricyclohexylphosphine
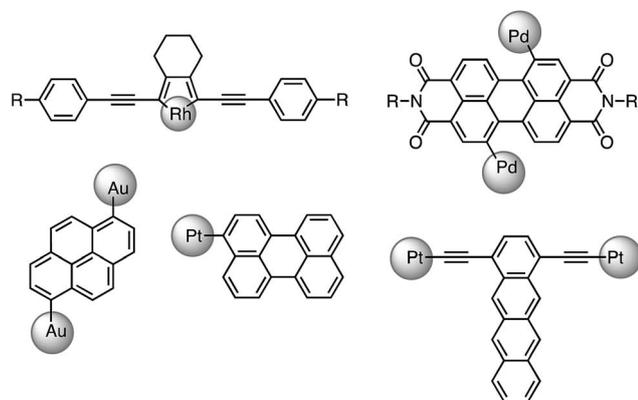

Chart 1 Au(I) and Au(III) acetylide complexes studied in this work.

Fig. 1 Selected examples of transition-metal complexes that display dominant fluorescence instead of phosphorescence. Auxiliary ligands coordinated to the metal ions are omitted.

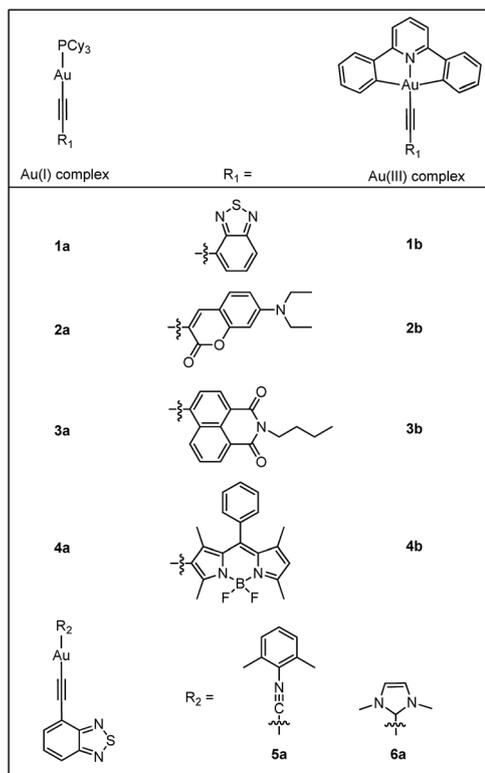(PCy$_3$) was used as the auxiliary ligand in these complexes because (1) it is optically transparent at wavelength >250 nm so that it is not involved in the emissive excited states in the UV-visible spectral region and (2) its steric bulkiness would prevent the gold ions from coming into close contact that could lead to low-lying excited states originated from metal–metal and π–π interactions. It is worth mentioning that several recently reported Au(I) alkynyl complexes bearing similar benzothiadiazole,[7] coumarin[8] and naphthalimide[9] derivatives also show similar luminescence properties as our Au(I) complexes.[10,11] The effects of auxiliary ligands on the photophysical properties of Au(I) complexes were also studied by comparing 1a with two derivatives containing 2,6-dimethylphenyl isocyanide (RNC, 5a) and 1,3-dimethylimidazol-2-ylidene (NHC, 6a) instead of the phosphine auxiliary ligand, respectively.

The effects of the oxidation state of the metal ion on the photophysical behaviours of transition-metal complexes are relatively unexplored. Herein, an analogous series of Au(III)-acetylides supported by the cyclometalated [C^N^C] ligand (1b–4b; HC^N^CH = 2,6-diphenylpyridine) were also prepared and their photophysical properties were compared with those of the Au(I) counterparts. The photophysical properties of both Au(I) and Au(III) complexes were investigated by steady-state and time-resolved spectroscopic measurements. DFT/TDDFT calculations were performed on the pairs (1a, 1b) and (4a, 4b) in order to understand the origin of the dramatic difference in ISC efficiencies between these Au(I) and Au(III) complexes.

Results

Synthesis and characterization

The gold(I) alkynyl complexes **1a–6a** were synthesized in 53–79% yields following the protocol of base deprotonation (NaOMe) of terminal alkynes and substitution of chloride ion of the corresponding Au(I) precursors.[5a,6a,b,12] As these complexes were observed to show signs of decomposition on SiO$_2$ column, column chromatography was not used for their purification. Analytically pure **1a–6a** were obtained by recrystallization from CH$_2$Cl$_2$/hexane mixtures. The Au(III) complexes **1b–4b** were synthesized by copper-catalyzed Sonogashira coupling between terminal alkynes and [Au(C^N^C)Cl] using deoxygenated CH$_2$Cl$_2$ as the solvent, with NEt$_3$ added to initiate the deprotonation of alkynes.[13] These complexes were purified by chromatography on SiO$_2$ column using dichloromethane and hexane as eluent. The yields were 51–84%.

All complexes have been characterized by ^{1}H and ^{13}C NMR, mass spectrometry (FAB+) and elemental analyses. Ligands L1–L4 were characterized by ^{1}H NMR and MS-EI. The complexes are stable in the solid state and in solution under ambient conditions. Complexes **1a–6a** are highly soluble in CH$_2$Cl$_2$ and THF but are less soluble in alcoholic solvents such as MeOH. Complexes **1b–4b** have lower solubility compared with their Au(I) counterparts. All of these gold complexes appear as yellow or orange solids except for **4a** and **4b** that are purplish red. The ^{31}P signals of **1a–4a** occur at *ca.* δ 56.3 as a singlet, characteristic of the ^{31}P signals of the Au–PCy$_3$ moiety that usually appear in the range of δ 56.0–58.0.[6a,b,12] In the ^{13}C NMR spectra, two doublets are observed at *ca.* δ 131.2–146.2 ($^2J_{CP} \approx 130$ Hz) and 94.6–98.4 ($^3J_{CP} \approx 24$ Hz) which can be assigned to the α and β-acetylenic carbons.[6a,b,12b] In **6a**, the carbene carbon ligated to gold occurs at δ 187.7.[14]

X-Ray crystallography

Crystals of **1a**, **4a** and **2b** were obtained by layering hexane over concentrated CH$_2$Cl$_2$ solutions. Their crystal data and selected bond lengths and angles are given in ESI.† Fig. 2 shows the structures of **1a** and **4a** (top panel). The P1–Au1–C(acetylide) angles of **1a** and **4a** are 175.0(13) and 178.1(2)° and Au1–C≡C angles are 170.9(4) and 177.6(5)°, respectively, revealing slight deviation from linear coordination geometry. The Au1–C(acetylide) distances of 2.049(4) and 2.001(5) Å and C≡C distances of 1.146(7) and 1.191(8) Å for **1a** and **4a**, respectively, are comparable with those of other reported gold(I) acetylide complexes.[6a,b,12a,b] The crystal packing diagrams of **1a** and **4a** are shown in ESI (Fig. S1†). In both cases, there are no short intermolecular contacts; the closest Au⋯Au distances are 5.9715(5) and 5.2726(4) Å for **1a** and **4a**, respectively.

The crystal structure of **2b** (Fig. 2, bottom) shows a slightly distorted square-planar geometry with C1–Au1–C17 angle of 162.44(14)°. The Au1–C(acetylide) and C≡C distances are 1.969(4) and 1.197(5) Å, respectively. These parameters are similar to those found in related cyclometalated Au(III) arylacetylide complexes.[13] The torsional angle between the Au(C^N^C) and arylacetylide planes is approximately 72.6°. This non-planarity gives rise to negligible π–π stacking between molecules as shown in Fig. S2 in ESI.†

Electrochemical properties

The electrochemical properties of selected complexes, **1a–4a** and **1b–4b**, were investigated by cyclic voltammetry. The electrochemical data are summarized in Table 1. The cyclic voltammograms of the Au(I) complexes and their Au(III) counterparts are shown in Fig. S3, ESI.† Except for **1a** and **2a**, both classes of complexes display both irreversible oxidation ($E_{pa} = +0.6$ to $+1.4$ V) and quasi-reversible/irreversible reduction waves ($E_{pc} = -1.5$ to -1.8 V) attributed to the redox process localized on the arylacetylides. For the pairs [2a, 2b] and [4a, 4b], the E_{pa} occur at relatively low potential of *ca.* +0.6 and +0.7 V, respectively, suggesting higher HOMO level of the conjugated coumarin and Bodipy than the other heterocyclic moieties. For the Au(III) complexes, other than the redox reactions occurring at the arylacetylide ligands at potentials similar to the Au(I) counterparts, there are also irreversible reduction waves at *ca.* −1.9 to −2.0 V attributable to reduction of the [C^N^C] ligands.
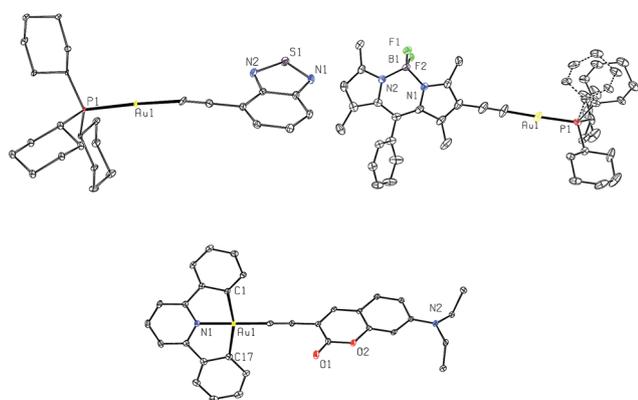

Fig. 2 Perspective drawings of the crystal structures of **1a** (top left), **4a** (top right) and **2b** (bottom) with the thermal ellipsoids shown at 30% probability level. Hydrogen atoms have been omitted for clarity.

Table 1 Electrochemical data of **1a–4a** and **1b–4b**[a]

Complex	$E_{pc}{}^{b}$/V	$E_{pa}{}^{c}$/V
1a	-1.79^{d}	—
2a	—	0.61, 0.95
3a	-1.61^{d}	1.44
4a	-1.50^{d}	0.71, 1.14
1b	$-1.82, -2.03$	1.25
2b	-1.89	0.59, 1.02
3b	$-1.59, -1.95$	1.42
4b	$-1.49^{d}, -2.02$	0.74

[a] Values determined in CH$_2$Cl$_2$ (Cp$_2$Fe$^{+/0}$ occurs at $E_{1/2} = +0.15$–0.16 V) at 298 K; values reported *versus* Ag/AgNO$_3$ reference electrode; electrolyte: 0.1 M *n*Bu$_4$NPF$_6$; scan rate = 100 mV s^{-1}. [b] Cathodic peak potential (E_{pc}) of irreversible wave. [c] Anodic peak potential of (E_{pa}) irreversible wave. [d] $E_{1/2} = E_{pa} + E_{pc}$ of quasi-reversible wave.

Table 2 Photophysical data of **1a–6a**, **1b–4b** and L1–L4[a]

	UV/Vis absorption, λ_{max}/nm ($10^3\varepsilon$/M^{-1} cm^{-1})	Emission						
		Medium	λ_F/nm	λ_{Ph}/nm	$\tau_{PF}{}^b$/ns	$\tau_{DF}{}^c$/μs	τ_{phos}/μs	$\Phi_{em}{}^d$
1a	265 (14.1), 275 (14.6), 305 (9.3), 311 (9.8), 319 (12.4), 379 (6.9)	CH$_2$Cl$_2$ 298 K	467	—	12.0	11.9	—	0.91
		Glassy 77 K	442	630, 688^e		n.d.^{f}	109^e	
		Solid 298 K	504	—		5.3	—	
		Solid 77 K	492	—		11.6	—	
2a	271 (13.9), 316 (3.2), 331 (3.2), 410 (40.0), 423 (3.7, br)	CH$_2$Cl$_2$ 298 K	466	596, 652^e	2.7	4.6 11.8^g	n.d.^{f} 13.6^g	0.70
		Glassy 77 K	460, 481	596, 653^e		243^e	203^e	
		Solid 298 K	405 (weak), 480 (sh), 515 (max)	598, 652 (sh)^e		15.0^e	24.6^e	
		Solid 77 K	409 (weak), 487 (max), 517 (sh)	597, 654(sh)^e		9.4^e	12.0^e	
3a	283 (12.2), 333 (5.6), 350 (11.3), 380 (23.8), 397 (25.5)	CH$_2$Cl$_2$ 298 K	441	613, 670^e	2.8	2.6, 12.5 31.5^g	n.d.^{f} 61.9^g	0.78
		Glassy 77 K	418, 439, 462 (sh)	569, 609, 666^e		n.d.^{f}	530^e	
		Solid 298 K	403 (sh), 503	610, 668^e		29.1	64.9^e	
		Solid 77 K	404 (sh), 504	627, 680^e		35.1	92.3^e	
4a	280 (13.5), 325 (4.5), 412 (10.1), 553 (40.2)	CH$_2$Cl$_2$ 298 K	593	—	0.8	—	—	0.04
5a	266 (18.6), 279 (15.8), 294 (12.5), 305 (11.2), 311 (10.1), 319 (12.7), 371 (7.1)	CH$_2$Cl$_2$ 298 K	456	—	11.0	6.8	—	0.90
6a	259 (18.3), 280 (17.5), 298 (7.8), 305 (10.7), 311 (11.4), 319 (14.2), 383 (8.3)	CH$_2$Cl$_2$ 298 K	476	—	14.0	7.4	—	0.84
1b	283 (20.4), 310 (24.1), 318 (26.8), 369 (13.0), 381 (13.8)	CH$_2$Cl$_2$ 298 K	461^h	630, 671 (sh)	13.8^h	—	104	0.003^i
		Glassy 77 K		610, 668			n.d.^{f}	
2b	312 (13.9), 406 (35.9, br), 432 (40.7)	CH$_2$Cl$_2$ 298 K	473^h	592, 642 (sh)	9.0^h	—	124	0.01^i
		Glassy 77 K		585, 605, 643			1200	
		Solid 298 K		530, 601, 660			1.4	
3b	312 (12.7), 325 (11.9), 379 (26.6), 395 (29.5)	CH$_2$Cl$_2$ 298 K	459^h	603, 659 (sh)	5.2^h	—	205	0.04^i
		Glassy 77 K		598, 614 (sh), 652			2200	
4b	312 (12.1), 320 (12.0), 366 (7.6), 384 (9.6), 401 (10.7), 515 (24.0, br), 546 (41.7)	CH$_2$Cl$_2$ 298 K	583	—	2.1	—	—	0.13
L1	303 (8.7), 309 (9.7), 316 (11.9), 341 (4.1)	CH$_2$Cl$_2$ 298 K	412	—	1.0	—	—	0.07
L2	260 (15.9), 326 (4.7), 405 (24.0, br), 417 (24.7)	CH$_2$Cl$_2$ 298 K	455	—	3.6	—	—	0.94
L3	333 (14.6), 350 (22.4), 367 (20.6)	CH$_2$Cl$_2$ 298 K	378, 398, 419 (sh)	—	0.5	—	—	0.11
L4	321 (3.9, br), 376 (5.3, br), 486 (14.8, sh), 517 (45.4)	CH$_2$Cl$_2$ 298 K	533	—	6.4	—	—	0.83

^{a} Data were obtained from steady-state measurements with degassed CH$_2$Cl$_2$ solutions (2×10^{-5} M) unless specified. Measurements with glassy solutions were performed in EtOH/MeOH (4 : 1) mixture at 77 K. ^{b} Emission lifetimes of prompt fluorescence (τ_{PF}) were determined by time-correlated single photon counting (TCSPC) measurement. ^{c} Emission lifetimes of delayed fluorescence (τ_{DF}) were obtained from fitting the decay of the time-resolved emission (TRE) as a mono-exponential decay in the delay time range of 0–40 ns and 1–46 μs, respectively. Measurements were performed in degassed CH$_2$Cl$_2$ (5×10^{-5} M) solutions. ^{d} Emission quantum yields (Φ_{em}) were obtained using quinine sulfate in degassed 0.5 M H$_2$SO$_4$ ($\Phi = 0.546$) as the standard unless specified. Φ_{em} measured in steady state is the overall emission quantum yield, i.e. $\Phi_{em} = \Phi_{PF} + \Phi_{DF}$ for **1a–3a** and **5a–6a**. ^{e} Obtained from time-resolved emission spectra. ^{f} Emission lifetime was not determined (n.d.) due to weak emission signal. ^{g} Determined from time-resolved emission spectra in degassed CH$_2$Cl$_2$ (1×10^{-5} M) solutions. ^{h} Determined from fs-TRF spectra. ^{i} Emission quantum yields (Φ_{em}) were obtained using [Ru(bpy)$_3$][PF$_6$]$_2$ in degassed acetonitrile as the standard ($\Phi = 0.062$).
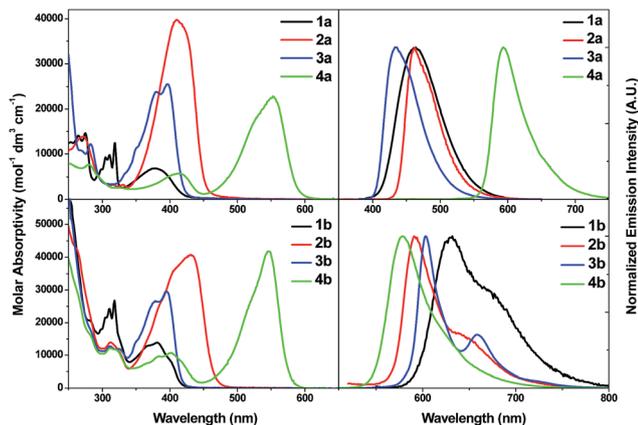
Fig. 3 UV-vis absorption spectra (left) and emission spectra (right) of **1a–4a** (top) and **1b–4b** (bottom) in CH_2Cl_2 at 298 K (2×10^{-5} M).

UV-vis absorption spectroscopy

All photophysical data of the gold complexes and the free ligands L1–L4 are listed in Table 2.

Electronic absorption of Au(I) complexes 1a–6a. Fig. 3 (top left) shows the absorption spectra of **1a–4a**. The lowest energy absorption bands of **1a–4a** are at 379, 410, 397 and 553 nm, respectively, and their molar absorptivities (ε) fall in the range 6.9×10^3 to 4×10^4 mol^{-1} dm^3 cm^{-1}. These lowest energy absorption bands have spectral features resembling those of L1–L4 (Fig. S4 in ESI†) and are attributable to the dipole-allowed intraligand transitions of the arylacetylide ligands ($^1\pi\pi^*(C\equiv CR)$) with some charge-transfer character. Similar assignments were also made for other Au(I) alkynyl complexes in the literature.[6,7,8a] Bathochromic shifts of ^{1}IL transitions of arylacetylides are observed upon coordination of the arylacetylides to the Au(I) ion and are ascribed to π-interaction between Au(I) 5d orbitals and the ligand π-orbitals (see MO surfaces in Fig. 9 and 10).

Replacing the neutral auxiliary ligand PCy_3 in **1a** with 2,6-dimethylphenyl isocyanide (RNC, **5a**) and 1,3-dimethylimidazol-2-ylidene (NHC, **6a**) results in a slight change in λ_{max} of the lowest energy absorption band ($\lambda_{max} = 371$ nm (**5a**, RNC) and 383 nm (**6a**, NHC) *cf.* $\lambda_{max} = 379$ nm (**1a**, PCy_3)) (Fig. S6 in ESI†).

Electronic absorption spectra of Au(III) complexes 1b–4b. Fig. 3 (bottom left) shows the UV-vis absorption spectra of the Au(III) complexes studied in the present work. The spectral features at $\lambda > 300$ nm are similar to those of the Au(I) analogues and free ligands L1–L4. Complexes **1b–4b** display low-energy absorption bands at $\lambda_{max} = 381, 432, 395$ and 546 nm, respectively, and with ε values in the range of 1.38×10^4 to 4.17×10^4 mol^{-1} dm^3 cm^{-1}. These absorption bands are, like the Au(I) complexes, attributable to $^1\pi\pi^*(C\equiv CR)$ transitions. Comparisons of the absorption spectra of **1a–4a** and **1b–4b** at $\lambda \leq 300$ nm revealed that the absorption bands in this spectral region are more intense in **1b–4b** with ε values of *ca.* 4×10^4 mol^{-1} dm^3 cm^{-1} and these high energy absorption bands likely involve intraligand $^1\pi\pi^*(C^\wedge N^\wedge C)$ transitions (Fig. S7 in ESI†).

Steady-state emission spectroscopy

All of the complexes are luminescent in degassed CH_2Cl_2 at room temperature and in 77 K glassy solutions (EtOH : MeOH = 4 : 1) upon excitation at the corresponding lowest-energy absorption λ_{max}. As depicted in Table 2, there is a distinct difference between the two classes of complexes: the Au(I) complexes **1a–6a** display predominantly fluorescence while the Au(III) complexes, **1b–3b**, exhibit exclusively weak phosphorescence. Complex **4b**, on the other hand, shows fluorescence only.

Emission of 1a–4a and 5a–6a. In dichloromethane solutions, structureless emission bands are observed at $\lambda_{max} = 467, 466, 439$ and 553 nm for **1a–4a**, respectively (Fig. 3, top right). The corresponding excitation spectra of **1a–4a** can be found in the ESI (Fig. S8†). The emission quantum yields for **1a–3a** are high ($\Phi_{em} = 0.91, 0.70$ and 0.78, respectively). In the case of **4a**, its emission quantum yield is low ($\Phi_{em} = 0.04$). Emission lifetimes of **1a–4a** are in the nanosecond time regime: 0.8–12 ns. As the emissions of these Au(I) complexes resemble those of the corresponding free ligands L1–L4, they are attributable to $^1\pi\pi^*(C\equiv CR)$ excited states, with some charge transfer character, which probably arise from mixings of metal-to-ligand charge-transfer (MLCT) character. Solvent effects on the emissions of **1a–3a** can be found in Fig. S10, ESI.† There is no discernible phosphorescence for **1a–4a** under steady-state conditions in solutions at either room temperature or 77 K (Fig. S9, ESI†).

Comparing the three Au(I) complexes bearing the benzothiadiazole moiety, the emission energies ($\lambda_{max} = 467, 456$ and 476 nm for **1a** (PCy_3), **5a** (RNC) and **6a** (NHC), respectively (Fig. S11 in ESI†)) and emission lifetimes ($\tau_{PF} \sim 11$–14 ns) are similar, indicating that the auxiliary ligand plays an insignificant role in modification of the electronic structures of the excited states.

Emission of 1b–4b. Emission spectra of the Au(III) complexes are depicted in Fig. 3 (bottom right). Contrary to the Au(I) analogues where the emission profiles are structureless, the emission spectra of complexes **1b–3b** are vibronically structured with λ_{max} at 630, 592 and 603 nm and quantum yields of 0.003, 0.01 and 0.04, respectively. The emission lifetimes are of hundreds of microseconds ($\sim$100 μs for **1b** and **2b**; $\sim$200 μs for **3b**). Taking into account the large Stokes shifts (between 6300 and 10 400 cm^{-1}), structured emission profiles, and long emission lifetimes, the emissions of **1b–3b** could be attributed to $^3\pi\pi^*(C\equiv CR)$ excited states with negligible mixings of MLCT and LLCT character (LLCT = ligand-to-ligand charge transfer). Solvent effects on the emissions of **1b** can be found in Fig. S12, ESI.† On the contrary, **4b** shows emission with a small Stokes shift of 920 cm^{-1} and emission lifetime of only 2.1 ns. Thus, the emission of **4b** is derived from fluorescence with $^1\pi\pi^*(C\equiv CBodipy)$ parentage.

Time-resolved spectroscopies for the gold(I) complexes

Nanosecond time-resolved emission (ns-TRE) spectra of the Au(I) complexes in degassed CH_2Cl_2 solutions at 298 K (5×10^{-5} M) are measured at different time delays and are presented in Fig. 4 (**1a**) and ESI (**2a–3a**, **5a–6a**; Fig. S13†). There are two
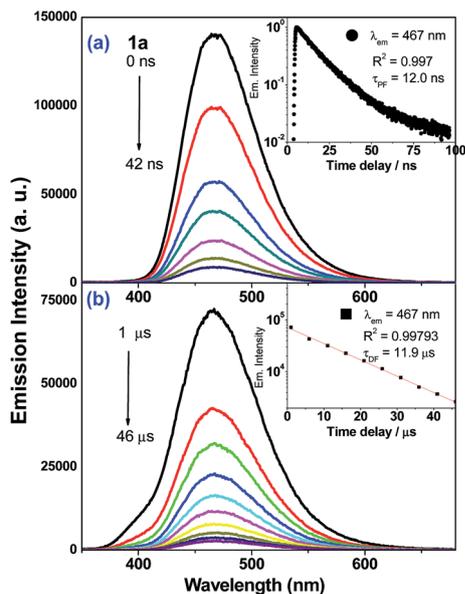
Fig. 4 ns-TRE spectra of **1a** recorded from (a) 0–42 ns and (b) after a time delay of 1 μs in degassed CH_2Cl_2 (5×10^{-5} M) at 298 K. Inset shows the emission kinetic decay trace. Decay time constants were fitted as mono-exponential decay (λ_{exc} = 355 nm).

components in the emission decay: a major component which decays within nanoseconds (τ_1 = 12.0 (**1a**), 2.7 (**2a**), 2.8 (**3a**), 11.0 (**5a**) and 14.0 ns (**6a**)) and a minor component with microsecond decay lifetime (τ_2 = 11.9 (**1a**), 4.6 (**2a**), 2.6, 12.5 (**3a**), 6.8 (**5a**) and 7.4 μs (**6a**)). For each of these Au(I) complexes, both decay components have identical emission profile and peak energy and so, the short-lived one (τ_1) is assigned to be prompt fluorescence (PF) while the long-lived one (τ_2) is delayed fluorescence (DF) of $^1\pi\pi^*$(C≡CR) character. In the case of **4a**, only PF (τ_{PF} = 0.8 ns) is observed. The proportion of DF and PF constituting the total emission of **1a–3a** have been estimated (Table 3): the intensity of DF is minute (<3%) when compared with that of PF (>97%). It is noted that delayed fluorescence in the microsecond time regime is indicative of the emission generated from a long-lived excited state. This is further supported by nanosecond transient absorption (ns-TA) measurements that reveal the presence of long-lived absorbing species in the microsecond timescale (*vide infra*).

Table 3 Proportion of PF and DF constituting the fluorescence of **1a–3a**[a]

Complex	% PF	% DF
1a	99.2	0.81
2a	99.9	0.1
3a	97.1	2.9

[a] % PF and % DF are estimated by integrating the emission intensity of degassed CH_2Cl_2 (5×10^{-5} M) in the spectral region of λ = 350–700 nm over the time range: 0–500 ns and 800 ns to 999 μs, respectively (λ_{exc} = 355 nm).

Weak phosphorescence bands were observed for **1a–3a** under different conditions. For dilute CH_2Cl_2 solutions (1×10^{-5} M) at 298 K, dominant emissions were observed in the spectral region of 440–470 nm, which correspond to fluorescence (Fig. S14, left panel in ESI†). In addition, weak emission peaks at *ca.* 600 nm become discernible for **2a** and **3a** and the lifetimes measured are 13.6 and 61.9 μs, respectively (Fig. S13, right panel in ESI†). Cooling to 77 K gives more resolved phosphorescence bands with vibrational progression spacings of 1300–1400 cm^{-1} for all three complexes (Fig. 5 and 6). For **1a**, contrary to the ns-TRE spectra recorded in degassed CH_2Cl_2 at room temperature (Fig. 4 (5×10^{-5} M); Fig. S14, ESI† (1×10^{-5} M)) where only DF could be observed over the time range 1–46 μs, in 77 K glassy solution, phosphorescence at 630 nm is dominant and the weak DF at 467 nm vanishes after 80 μs (Fig. 5a). The phosphorescence band decays with first-order kinetics at τ_{phos} = 109 μs. Similarly, the low-temperature ns-TRE spectra of **3a** is dominated by phosphorescence at 609 nm and DF vanishes after 200 μs (Fig. 5b). The phosphorescence band also decays mono-exponentially with τ_{phos} = 530 μs. The photodynamics of **2a** at 77 K, however, is different from that of **1a** and **3a**: both DF and phosphorescence of **2a** are of comparable intensities initially (∼1 μs) in the 77 K ns-TRE spectra (Fig. 6); in addition, DF and phosphorescence do not follow first-order kinetics but decay according to the power law ($I \propto t^{-1}$) in the time interval 1 μs to 1.2 ms (inset of Fig. 6). The thermally induced Stokes shifts ($\Delta E_s = E_{00}$ (77 K) $- E_{00}$ (298 K)), being ∼0 (**2a**) and ∼107 cm^{-1} (**3a**), are small, thus supporting that the phosphorescence bands are originated from ^{3}IL.[15] Moreover, as the emission energies and profiles of the low-energy bands are similar to those of the steady-state emission
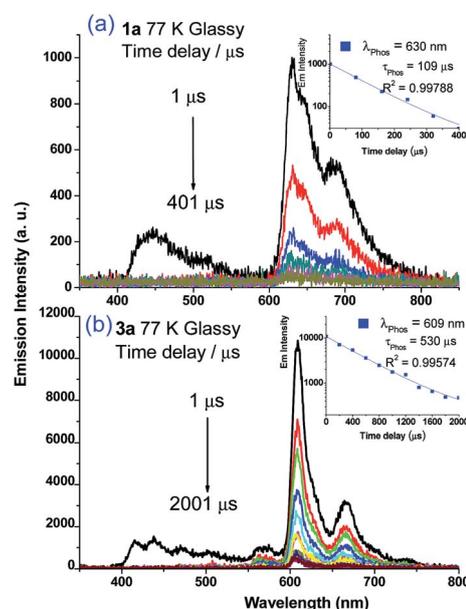

Fig. 5 ns-TRE spectra of (a) **1a** and (b) **3a** in 77 K glassy solution (EtOH/MeOH = 4 : 1) recorded at different time intervals. λ_{exc} = 355 nm; integration time: 80 and 200 μs for **1a** and **3a**, respectively. Insets of (a) and (b) show the kinetic decay traces at the specified wavelengths with the estimated phosphorescence lifetime (τ_{phos}).
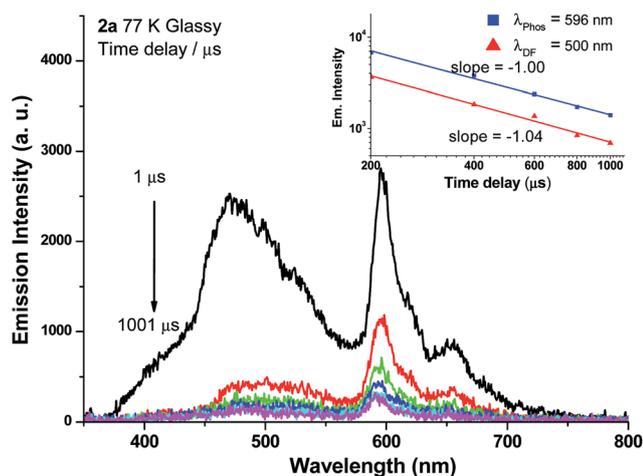
Fig. 6 ns-TRE spectra of **2a** in 77 K glassy solution (EtOH/MeOH = 4 : 1) recorded at different time intervals. λ_{exc} = 355 nm; integration time: 200 μs. Inset shows the log–log plot of emission intensity of DF (λ_{DF} = 500 nm) and phosphorescence (λ_{phos} = 596 nm) of **2a** in 77 K glassy solution against time; both decay according to a power law: $I \propto t^{-1}$.

spectra of the Au(III) analogues, the low-energy emission bands of **1a–3a** are assigned to be from phosphorescence decay of the $^3\pi\pi^*$(C≡CR) excited state.

Nanosecond transient absorption (ns-TA) difference spectra of **1a–3a** (Fig. 7) and **5a–6a** (Fig. S15 in ESI†) have been recorded in deoxygenated CH_2Cl_2 at a gate delay of 1 μs after excitation at λ = 355 nm. The ns-TA spectra are characterized by an intense positive signal due to excited-state absorption (ESA) within the spectral range 400–700 nm. The decay time constants of the lowest-energy ESA (τ_{ESA}) are 20.3 (**1a**), 39.2; 304 (**2a**), and 13.3; 70.9 μs (**3a**) (insets of Fig. 7). Changing the auxiliary ligand from PCy$_3$ (**1a**) to RNC (**5a**) and NHC (**6a**) results in negligible changes in the ns-TA spectra and τ_{ESA} (Fig. 7 vs. S15†), suggesting that auxiliary ligand has little effect on the photophysics of the gold(I) arylacetylide complexes.

Time-resolved spectroscopies for the gold(III) complexes

ns-TRE and ns-TA difference spectra of **1b–3b** have been recorded in degassed CH_2Cl_2 solutions at 298 K at a gate delay of 1 μs. The

ns-TRE spectra of **1b–3b** (Fig. S16 in ESI†) have the same emission profiles and peak positions as the corresponding steady-state phosphorescence spectra and exhibit single exponential decay lifetimes of 20.8 (**1b**), 9.7 (**2b**) and 18.3 μs (**3b**). For the ns-TA difference spectra of **1b–3b** (Fig. 8, bottom panel), a broad positive ESA band was observed in the spectral region 450–800 nm; this ESA signal follows first-order kinetics with lifetimes determined to be 23.8 (**1b**), 13.6 (**2b**) and 25.4 μs (**3b**), in reasonable agreement with the phosphorescence decay lifetimes determined from their respective ns-TRE spectra, thus indicating that the broad ESA is derived from $T_1 \rightarrow T_n$ absorption.

To probe the early excited state dynamics of the gold(III) complexes, in particular the events associated with ISC, femtosecond time-resolved fluorescence (fs-TRF) and transient absorption difference spectra (fs-TA) of **1b–3b** have been recorded. Fig. 8 depicts the fs-TRF (top panel) and fs-TA spectra (middle panel) of complexes **1b–3b** in CH_2Cl_2 solution at various time intervals after 400 nm excitation at 298 K. Promptly (<2 ps) after photo-excitation, an unstructured fluorescence band peaking at 461 (**1b**), 473 (**2b**) and 459 nm (**3b**) appears and decays completely within 100 ps. As the TRF emission peaks and profiles closely resemble those of their Au(I) analogues, **1a–3a**, these TRF spectra are suggested to be originated from the $^1\pi\pi^*$(C≡CR) excited state. Fitting of the kinetic traces at their peaking wavelengths reveals that bi-exponential functions are required for **1b–3b** with τ_1 and τ_2 being 1.28 and 13.8 ps for **1b**, 0.95 and 9.04 ps for **2b**, and 0.74 and 5.22 ps for **3b**.

In the fs-TA of **1b–3b** (Fig. 8, middle panel), all three complexes displayed similar spectral transformations: the initially formed (~1.4–2.5 ps) excited state absorption peaking at ~490 nm (ESA1) decays with a concomitant growth of a broad band covering a spectral region 450–800 nm (ESA2) and is fully developed within 40 ps and persists up to 2.7 ns (the longest time recorded in the fs measurements). Clear isosbestic points could be observed at ~500 nm (**1b**), 530 nm (**2b**) and ~500 and 700 nm (**3b**) during the temporal evolution. Such kind of spectral conversion points to a precursor–successor relationship between ESA1 and ESA2. Kinetic analyses at representative wavelengths of these TA spectra reveals that ESA1 of **1b** and **3b** decay bi-exponentially with τ_1 and τ_2 being 0.80 and 13.2 ps for **1b** and 0.63 and 3.49 ps for **3b**, respectively, whereas ESA1 of **2b** decays with a single exponential time constant of τ_2 = 8.38 ps.
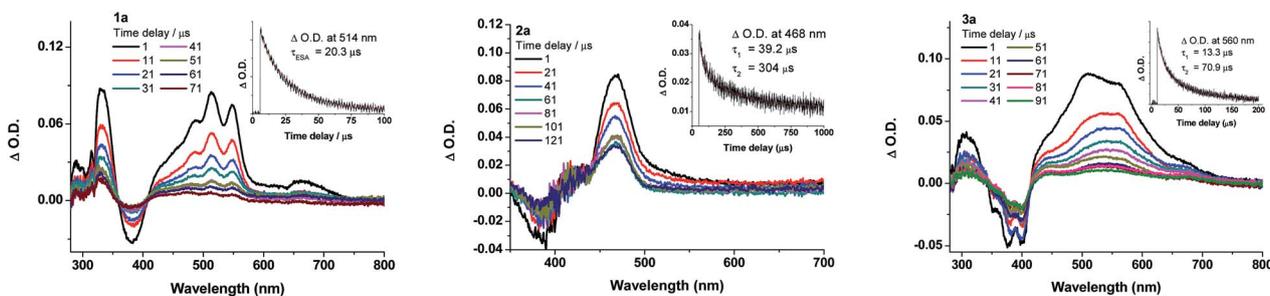

Fig. 7 Nanosecond transient absorption (ns-TA) difference spectra of **1a–3a** recorded at selected decay times in degassed CH_2Cl_2 (5×10^{-5} M) at 298 K. Insets show the ESA kinetic decay trace at the specified wavelengths; decay lifetimes were fitted as mono-exponential decay for **1a** and bi-exponential decays for **2a** and **3a**. (λ_{exc} = 355 nm; integration time: 200 ns).
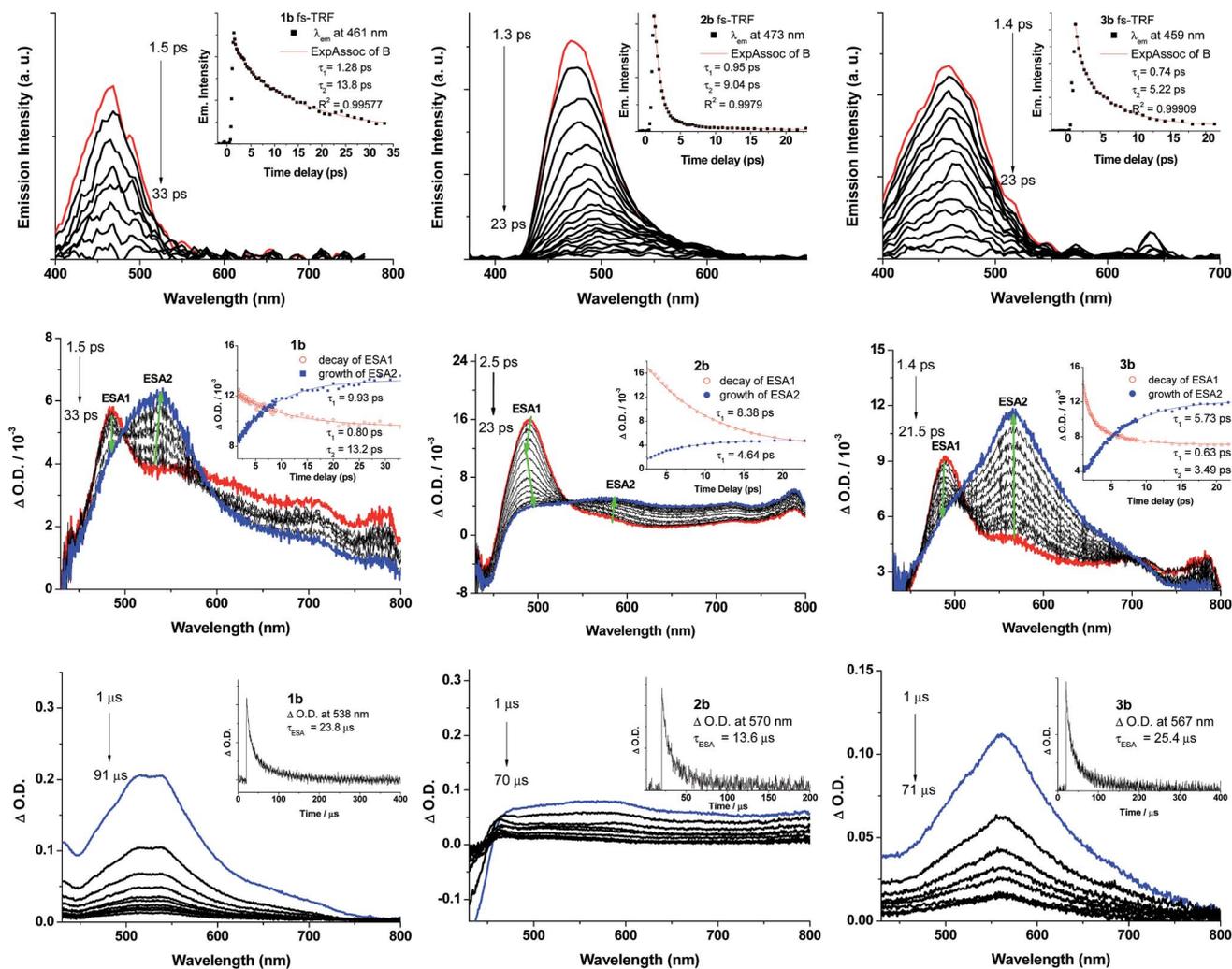
Fig. 8 (Top) fs-TRF spectra and (middle) fs-TA difference spectra of **1b–3b** in CH$_2$Cl$_2$ (5×10^{-5} M) at 298 K (λ_{exc} = 400 nm; 120 fs fwhm). Arrows indicate the spectral evolution. (Bottom) ns-TA difference spectra of **1b–3b** in degassed CH$_2$Cl$_2$ (laser λ_{exc}: 355 nm). Insets show the kinetic time profiles and the decay time constants at the specified wavelengths.

ESA2, on the other hand, grows with first-order kinetics for all three complexes **1b–3b** with time constants τ_{ESA2} = 9.93 (**1b**), 4.64 (**2b**) and 5.73 ps (**3b**). Given the similar decay time constants between the fs-TRF and ESA1 in fs-TA of **1b–3b**, the spectral dynamics for both time-resolved spectra should be originated from the same S$_1$ excited state, namely, the $^1\pi\pi^*$(C≡CR) excited state as revealed in the fs-TRF. On the other hand, comparing the ESA2 in fs-TA spectra at the longest time recorded with the corresponding ns-TA spectra for each Au(III) complex (Fig. 8, bottom panel), the two spectra are similar, indicating that ESA2 is derived from T$_1$ → T$_n$ absorption. Because there is a precursor–successor relationship between the ESA1 (S$_1$ → S$_n$ absorption) and ESA2 (T$_1$ → T$_n$ absorption), τ_2 of ESA1 is assigned to ISC from the S$_1$ excited state to a receiving triplet excited state, which then internally converted to the T$_1$ excited state with an ultrafast time scale. Thus, τ_{ISC} = 13.2 ps (**1b**), 8.38 ps (**2b**) and 3.49 ps (**3b**). The short τ_1 = 0.80/1.28 (**1b**), 0.95 ps (**2b**) and 0.63/0.74 ps (**3b**) of ESA1/TRF may likely correspond to the S$_1$ vibrational relaxation.

Intersystem crossing rate

The spectroscopically determined intersystem crossing rate constants (k_{ISC}) and the corresponding time constants (τ_{ISC}) for both Au(I) and Au(III) complexes studied herein are tabulated in Table 4. For **1a–3a** and **5a–6a**, assuming that the major non-

Table 4 k_{ISC} and τ_{ISC} of the Au(I) and Au(III) complexes

Complex	$k_{ISC}{}^a$/10^7 s^{-1}	$\tau_{ISC}{}^b$/ns	Complex	$k_{ISC}{}^b$/10^{10} s^{-1}	$\tau_{ISC}{}^c$/ps
1a	<0.75	133	**1b**	7.57	13.2
2a	<11.1	9.0	**2b**	11.9	8.38
3a	<7.9	12.7	**3b**	28.7	3.49
5a	<0.91	110			
6a	<1.14	87.5			

^{a} k_{ISC} for **1a–3a**, **5a–6a** are calculated according to eqn (1). ^{b} τ_{ISC} = 1/k_{ISC}. ^{c} τ_{ISC} of **1b–3b** is estimated from τ_2 obtained from the fs-TA spectra of ESA1.

radiative decay of the S_1 excited state is ISC, *i.e.* $k_{nr} \approx k_{ISC}$, an upper bound approximation of the k_{ISC} values could be obtained by eqn (1):

$$\Phi_{em} = \frac{k_r}{k_r + k_{ISC}} \qquad (1)$$

The estimated k_{ISC} for the gold(I) complexes are 7.5×10^6 to 1.1×10^8 s^{-1} and the intersystem crossing time constants (τ_{ISC}) are 9.0–133 ns. These τ_{ISC} are much larger than those of many phosphorescent transition-metal complexes (τ_{ISC} in the femtosecond to picosecond timescale). For **1b–3b**, the τ_{ISC} values are more than three orders of magnitude faster than their gold(I) analogues; these ISC rates, nevertheless, are comparable to other transition-metal complexes where $S_1 \rightarrow T_1$ ISC is mediated by a higher-lying T_n triplet excited state.[16,17]

Computational study

The different luminescence behaviors between the Au(I) and Au(III) systems were investigated by DFT/TDDFT calculations. The pair (**1a**, **1b**) was chosen as a representative example to examine why the Au(I) complexes studied herein display only fluorescence while the Au(III) counterparts exhibit exclusively phosphorescence. As the Bodipy-functionalized complexes give fluorescence for both Au(I) and Au(III) complexes, DFT/TDDFT calculations were also performed on the pair, (**4a**, **4b**). To save computational time, the cyclohexyl groups of the phosphine ligands in **1a** and **4a** were replaced by methyl groups.

Calculations on 1a and 1b

The frontier MO diagrams of **1a** and **1b** are shown in Fig. 9. The HOMO and LUMO for both complexes **1a** and **1b** are predominantly localized on the arylacetylide ligand. For **1b**, a considerable contribution (17%) from the C^N^C moiety to the LUMO is also noted. The energy gap between HOMO and H−1 in **1a** is approximately 0.88 eV. For **1a**, the H−1 is comprised of the antibonding combinations of Au(d_{xy}) and π(C≡C) orbitals with little

involvement of the phosphine ligand. For **1b**, H−1 is composed of Au(d_{xz}) and the π(C^N^C) orbitals; the energy gap between HOMO and H−1 in **1b** is only 0.2 eV. The H−2 of **1b** is made up of an antibonding combination of the Au(d_{xy}), π(C≡C) and σ(C^N^C) orbitals, with a HOMO/H−2 orbital energy gap of only ~0.4 eV. Clearly, the cyclometalated [C^N^C] ligand has a role in destabilizing the Au(d) orbitals. Therefore, the HOMO and H−1/H−2 energy gaps in **1b** are much smaller than that in **1a**.

The energies of the singlet and triplet excited states and the associated nature and composition for **1a** and **1b** at their respective optimized singlet ground state geometries are obtained by TDDFT and are shown in Table S5 and S6 in ESI.† For **1a**, there is only one triplet excited state (T_1) which is more than 10 000 cm^{-1} below S_1. In addition, both S_1 and T_1 excited states are of the same parentage and are derived from HOMO → LUMO transition (~90%) and thus, there would be no effective SOC between them. The triplet excited states above S_1 were also considered; the closest lying T_m excited state with efficient SOC is when $m = 4$, which is derived from a H−1 to LUMO transition (90% H−1 → L). However, the energy separation $\Delta E(S_1$–$T_4)$ is −3180 cm^{-1}, which is too large to be overcome by thermal activation.

On the other hand, for **1b**, there are four triplet excited states which are lower-lying than S_1, of which the closest-lying T_4 excited state is only ~70 cm^{-1} below the S_1 excited state. Thus, thermal energy at room temperature assists facile ISC, even though SOC is small between the S_1 and T_4 excited states ($|<S_1|H_{SOC}|T_4>|^2 \sim 1.5$ cm^{-2}). In addition, among the triplet excited states above S_1, there is a close-lying T_5 excited state derived from the H−2 → LUMO transition (79%) which lies only 390 cm^{-1} above the S_1 excited state and ISC from S_1 to T_5 could be thermally activated. Besides, owing to the different orientations of the d-orbitals in HOMO and H−2, the S_1 and T_5 excited states could have effective SOC ($|<S_1|H_{SOC}|T_5>|^2 \sim 4.1 \times 10^3$ cm^{-2}).

Calculations on 4a and 4b

The Frontier MOs for **4a** and **4b** are shown in Fig. 10. Relative to **1a** and **1b**, the HOMO is destabilized and the LUMO is stabilized

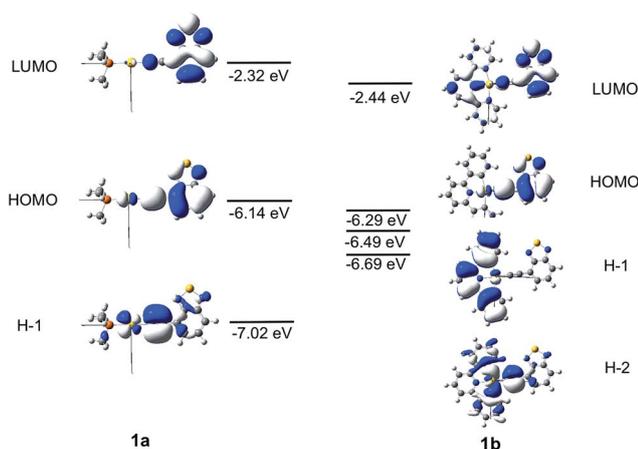
Fig. 9 Frontier MOs of **1a** and **1b** at the optimized S_0 geometries. Orbital energies are also given in eV.
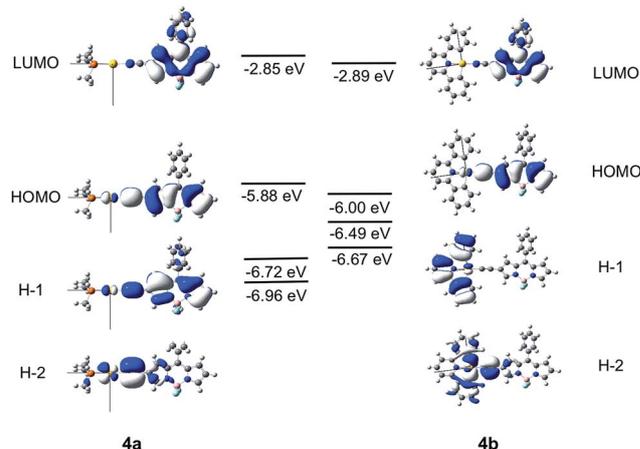

Fig. 10 Frontier MOs of **4a** and **4b** at their optimized S_0 geometries. Orbital energies are also given in eV.

for **4a** and **4b**. Even for **4b**, which contains a cyclometalated [C^N^C] ligand, the LUMO is predominantly localized on the Bodipy-functionalised arylacetylide ligand. The HOMO is composed of an antibonding combination of the $Au(d_{yz})$ and $\pi(C\equiv CBodipy)$ orbitals. The energies and compositions of the singlet and triplet excited states of **4a** and **4b** at their respective optimized singlet ground state geometries were obtained by TDDFT and are collected in Tables S7 and S8 in ESI.† For this pair, (**4a**, **4b**), the two triplet excited states, T_1 and T_2, are more than 2000 cm^{-1} below the S_1 excited state and are all composed of $Au(d_{yz})$ orbitals. As SOC between the coupling singlet and triplet excited states would be ineffective with d-orbitals of the same orientation, ISC from S_1 to T_2 (or T_1) for **4a** and **4b** would be sluggish.

For **4a**, the T_3 excited state is the closest-lying triplet excited state that could have effective SOC with the S_1 excited state due to a minor contribution of the $H-5 \rightarrow$ LUMO transition to the T_3 excited state ($H-5$ is composed of the $Au(d_z^2)$ orbital); however, $\Delta E(S_1-T_3)$ is -2955 cm^{-1} (negative sign indicates that T_3 lies above S_1) which is much larger than the thermal energy. For **4b**, the T_3 excited state is also the closest-lying triplet excited state that could have effective SOC with the S_1 excited state due to a minor contribution of $H-1 \rightarrow$ LUMO transition in the T_3 excited state (the d-orbitals of the Au(III) ion at the HOMO and $H-1$ of **4b** are of different orientations, Fig. 10). However, the singlet–triplet gap, $\Delta E(S_1-T_3) = -1192$ cm^{-1}, is also much larger than the thermal energy. Thus, the pair (**4a**, **4b**) is expected to have slow ISC rates, when taking into consideration both the singlet–triplet energy gaps and SOC.

Discussion

General remarks on the photophysical properties

The emissions of the Au(I) complexes, **1a–6a** are attributable to ^{1}IL $\pi\pi^*(C\equiv CR)$ excited states. Pronounced red shifts in emission λ_{max} of arylacetylides can be observed upon their coordination to Au(I) ion (*e.g.* $\lambda_{max} = 412$ nm (L1) *vs.* 467 nm (**1a**)). Considering the complexes **1a**, **5a** and **6a**, which have different neutral auxiliary ligands (phosphine (PCy$_3$, **1a**), isocyanide (RNC, **5a**) and N-heterocyclic carbene (NHC, **6a**)) but the same acetylide ligand with a benzothiadiazole moiety, the lowest energy emission λ_{em} red shifts with the auxiliary ligand from 456 nm (RNC) to 467 nm (PCy$_3$) to 476 nm (NHC). A rationalization would be that the NHC, being the strongest σ-donor ligand among the auxiliary ligands in the three complexes, destabilizes the Au(d) orbital to the greatest extent. From DFT calculations, the HOMO is comprised of a Au(d) orbital and $\pi(C\equiv CR)$ (Fig. 9). Thus, the more electron-donating the auxiliary ligand, the more destabilized the HOMO, and hence, the smaller the HOMO–LUMO gap and the $^1\pi\pi^*(C\equiv CR)$ energy. A similar trend in the lowest energy absorption λ_{abs} can also be observed on changing the auxiliary ligand from RNC (371 nm) to PCy$_3$ (379 nm) and NHC (383 nm).

Most of the reported luminescent cyclometalated Au(III) complexes display phosphorescence that comes from the $^3\pi\pi^*$ IL excited state localized on the cyclometalated ligands.[13] For the Au(III) complexes studied herein, **1b–3b**, the lowest-

energy triplet excited states are of $^3\pi\pi^*(C\equiv CR)$ in nature, with $\lambda_{max} = 630$, 592 and 603 nm respectively. These complexes, however, exhibit rather weak phosphorescence, with Φ_{em} values in the range of 0.003–0.04. It is noted that in 77 K glassy solutions, the phosphorescence lifetimes are significantly increased compared with those obtained in degassed CH$_2$Cl$_2$ at RT (*e.g.* 205 μs at RT to 2.2 ms at 77 K for **3b**). Since low temperature and rigid glassy matrix can impede structural distortion, the lifetimes obtained at 77 K could reflect the intrinsic radiative lifetime of the complexes. The especially long emission lifetimes can reflect the predominant localization of the emitting T_1 excited state on the arylacetylide ligand, *i.e.* $^3\pi\pi^*(C\equiv CR)$ with little participation of the metal ion. This is also corroborated by the small thermally induced Stokes shifts ($\Delta E_s = E_{00}$ (77 K) $- E_{00}$ (298 K)) of less than 600 cm^{-1} (Table 2).

Intersystem crossing in gold(I) and gold(III) complexes

ISC is usually fast in transition-metal complexes with time constants (τ_{ISC}) in the fs to ps time regimes. In the literature, there are numerous examples which show ultrafast ISC,[1,18–25] *e.g.* [M(bpy)$_3$]$^{2+}$ (M = Ru or Fe, $\tau_{ISC} = 30$ fs),[19a,b] [Re(L)(CO)$_3$(bpy)] ($\tau_{ISC} = 100$–140 fs),[20] [Ir(piq)$_3$] (piq: 1-phenylisoquinoline; $\tau_{ISC} = 70$ fs),[21b] [Pt(PBu$_3$)$_2$(C$\equiv$CPh)$_2$] ($\tau_{ISC} = 70$ fs),[22] and [Cy$_3$PAu(2-naphthyl)] ($\tau_{ISC} = 230$ fs)[23] *etc.* These τ_{ISC} correspond to rates of intersystem crossing (k_{ISC}) in the range of 10^{12} to 10^{13} s^{-1}. The fast k_{ISC} in transition-metal complexes is traditionally attributed to a large spin–orbit coupling (SOC) constant inherited from the heavy metal atom. However, there are increasing number of reports revealing slow ISC rate ($k_{ISC} \sim 10^8$ s^{-1}) in spite of the presence of heavy transition metal, such as the cases of Rh(I)- and Ir(III)-bis(arylethynyl)cyclopentadiene,[3] Au(I)-pyrene,[4b] Pt(II)-perylene/[4c] tetracene,[4e] and Pd(II)-perylene diimide;[4f] all these complexes contain highly conjugated ligand systems and display ligand-dominated $^1\pi\pi^*$ fluorescence. There are also cases where comparable k_{ISC} and k_r of $S_1 \rightarrow S_0$ leads to the observation of dual fluorescence–phosphorescence under steady-state condition, *e.g.*, [Pt(L)(acac)] and [Ir(L)(acac)] (L = 2-(oligothienyl)pyridine);[26] [Os(L)(CO)$_3$X] (L = 8-quinolinolate[27] or isoquinoline-triazole),[28] and [Bu$_4$N]$_4$[Pt$_2$(μ-P$_2$O$_5$(BF$_2$)$_2$)$_4$],[29] *etc.*

In this work, the luminescence behaviour of the Au(I) and Au(III) complexes are drastically different, even though they have the same metal and arylacetylide ligands. Ligand-dominated fluorescence has been observed with the Au(I) complexes, **1a–3a** and **5a–6a**, with k_{ISC} estimated to range from 7.5×10^6 to 1.1×10^8 s^{-1}. The Au(III) complexes **1b–3b**, on the other hand, display phosphorescence, with k_{ISC} estimated to be larger than 10^{10} s^{-1}. The major difference between the two series of gold complexes is the oxidation state of Au ion, that dictates the coordination geometry, *i.e.* a linear geometry for the Au(I) complexes, **1a–6a**, and a square-planar geometry for Au(III) complexes, **1b–4b**. The coordination geometry has a significant impact on the relative energies of the frontier orbitals (specifically, the d-orbital energies) and hence the relative energies of the singlet and triplet excited states, which subsequently affect the k_{ISC}.

The two factors that determine the k_{ISC} are (1) the SOC matrix element $<S_n|H_{SOC}|T_m>$, and (2) the energy gap (ΔE_{ST}) between the coupling singlet (S_n) and triplet (T_m) excited states. The larger the H_{SOC} and the smaller the energy gap (ΔE_{ST}), the faster will be k_{ISC}. For effective SOC, this requires the metal d-orbitals of the coupling singlet and triplet excited states to have different orientations. For example, if S_n is derived from a metal-to-ligand charge transfer (MLCT) excited state where $Au(d_{xz})$ orbital is involved, H_{SOC} would be zero if the triplet excited state is also an MLCT state that involves $Au(d_{xz})$ orbital because of symmetry reasons.

The pair (**1a**, **1b**) has been chosen as a representative example to illustrate the different photophysical properties exhibited by the Au(I) and Au(III) arylacetylide complexes studied in this work. From the DFT/TDDFT calculations, it is revealed that owing to the inherent linear coordination geometry of the Au(I) complex, the d-orbitals of the gold(I) ion is mainly destabilized by the arylacetylide ligand (Fig. 9 and Table S9 in ESI†). On the other hand, as Au(III) complexes are assumed to have a square-planar four-coordinated geometry, thus, in addition to the antibonding interactions with the arylacetylide ligand, the d-orbitals of gold(III) ion could also be destabilized by the cyclometalated [C^N^C] ligand (both π-type, *e.g.* H−1, and σ-type, *e.g.* H−2 in **1b**; Fig. 9 and Table S9 in ESI†); these latter interactions result in smaller d-orbital splittings in the Au(III) series than the Au(I) series. In effect, S_1 and S_2 excited states are ∼4200 cm^{-1} apart for **1a** while the analogous splitting (between S_1 and S_3 excited states) is only ∼1300 cm^{-1} for **1b**. As S_2 of **1a** is derived from $^1[Au(d_{xy}) \rightarrow \pi^*(C{\equiv}CR)]/^1[\pi(C{\equiv}C) \rightarrow \pi^*(C{\equiv}CR)]$ (^{1}MLCT/^{1}ILCT) and S_3 of **1b** from $^1[Au(d_{xy}) \rightarrow \pi^*(C{\equiv}CR)]/^1[\pi(C{\equiv}C) \rightarrow \pi^*(C{\equiv}CR)]/^1[\pi(C^N^C) \rightarrow \pi^*(C{\equiv}CR)]$ (^{1}MLCT/^{1}ILCT/^{1}LLCT), *i.e.*, both are of charge-transfer type excited states, the singlet–triplet energy gaps for this type of transitions are small ($\Delta E(S_2–T_4) \sim 1000$ cm^{-1} for **1a** and $\Delta E(S_3–T_5) \sim 900$ cm^{-1} for **1b**) (T_4 (**1a**) and T_5 (**1b**) are the triplet counterpart of S_2 (**1a**) and S_3 (**1b**) respectively). As depicted in Fig. 11, the S_1/T_5 energy gap for **1b** is small but the S_1/T_4 energy gap for **1a** is large. In other words, the oxidation state of the gold ion affects the coordination geometry of the complex, which in turn change the interactions between the metal d-orbitals and ligand orbitals, giving rise to different d-orbital splitting and subsequently the singlet–triplet splitting (ΔE_{ST}) of the two coupling excited states in the gold complexes.

Moreover, DFT/TDDFT calculations also revealed that there is a triplet excited state (T_4) almost isoenergetic with the S_1 excited state (<70 cm^{-1} below the S_1 excited state) in **1b** such that even though the SOC between S_1 and T_4 is small due to the similar d-orbital orientations involved in both excited states, thermal energy could promote facile ISC. With **1a**, the closest triplet excited state (T_2) to the S_1 excited state is more than 500 cm^{-1} above the S_1 excited state, which is more than twice the thermal energy at room temperature and SOC is also small between these two excited states as the d-orbitals involved are also of the same orientations. Thus, taken together both the SOC and ΔE_{ST}, **1b** should have a much faster k_{ISC} than **1a**.

On the other hand, for the Bodipy-functionalized complexes, **4a** and **4b**, only $^1\pi\pi^*(C{\equiv}CBodipy)$ fluorescence

with no long-lived species are observed under ns-TRE and ns-TA measurements. The photophysical behavior of the Bodipy-functionalized complexes can be attributed to the intrinsically small band-gap of the Bodipy moiety. Due to the highly conjugated structure of Bodipy, the HOMO is much destabilized and there is a wide orbital energy gap between the HOMO and other occupied MOs, even in the case of **4b** which contains a [C^N^C] ligand. As a result, the HOMO/H−x orbital energy gap is the largest among the four arylacetylide ligands studied herein (H−x is the other occupied orbitals lower in energy than the HOMO; $x = 1, 2, …$). In effect, the closest T_m excited state that could have effective SOC with S_1 is more than 1000 cm^{-1} above the S_1 excited state. With such a large $\Delta E(S_1–T_m)$, thermal energy would be insufficient to promote ISC. Therefore, similar to the scenario in the case of **1a** (Fig. 11, left), ISC is sluggish for Au(I) and Au(III) arylacetylide complexes bearing Bodipy.

Mechanism for the generation of delayed fluorescence

From the ns-TRE measurements of **1a–3a**, DF contributes to the total fluorescence, though only a minute proportion (<3%, Table 3). In general, the mechanism of DF could be inferred from the dependence of the DF intensity (I_{DF}) with the power of excitation light.[30] According to Bässler, a quadratic dependence of excitation power with the DF intensity indicates that the mechanism of the DF is TTA with dominant phosphorescence.[30b] On the other hand, a linear dependence of DF intensity with excitation power could be due to three possible mechanisms: TTA with dominant delayed-fluorescence, TADF, and GP-recombination. As depicted in Fig. 12, the plot of I_{DF} against excitation intensity in double-logarithm scale gave a slope of 1.71 ≈ 2 for **1a**; this nearly quadratic dependence is most consistent with the TTA mechanism with dominant phosphorescence. However, for **2a** and **3a** (slope = 0.916 and 1.10), both display nearly linear dependence between I_{DF} and excitation intensity. Therefore, it is not possible to confirm the mechanism for DF in the case of **2a** and **3a** by solely considering the excitation power dependence.

Time-dependence of I_{DF} and phosphorescence intensity (I_P) could also give hints to the DF mechanism.[30,31] For TTA with dominant DF, phosphorescence intensity decays with a power law, $I_P \propto t^{-1}$ while I_{DF} is approximately constant at short time and $I_{DF} \propto t^{-2}$ at longer time. For the GP-recombination mechanism, both DF and phosphorescence decay in accordance with the power law, $I_{DF} \propto t^{-1}$, at both short and long times.[30a] In the case of **2a** in 77 K glassy solution, both DF and phosphorescence decayed according to the power law: $I \propto t^{-1}$ over the time intervals investigated (1 μs to 1.2 ms) (Fig. 6, inset), suggesting that the DF mechanism under this condition is most likely the GP-recombination mechanism. As for **3a**, there is no power law decay relation with both DF and phosphorescence and so it seems unlikely that GP-recombination is the mechanism for the generation of DF in **3a**. There is still not enough information to conclude on the DF mechanism for **3a**.
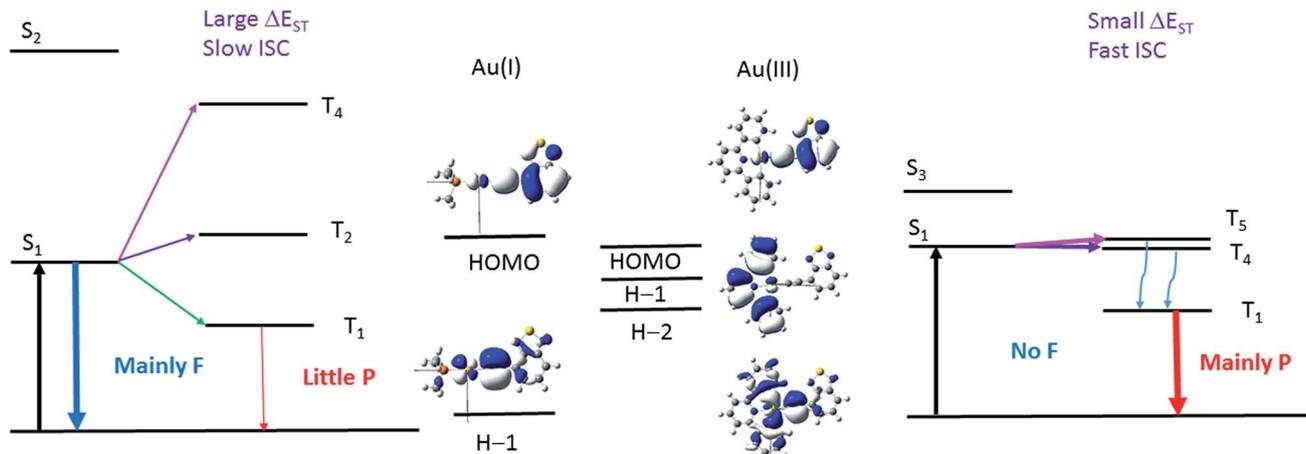
Fig. 11 Illustration of the low-lying singlet and triplet excited states of Au(I) (left) and Au(III) (right) complexes that accounts for the different photophysical behaviour of the Au(I) and Au(III) complexes investigated in this work. S_1 and T_1 for both complexes are derived from HOMO → LUMO transitions; S_2 and T_4 excited states of **1a** are derived from ^{1,3}[H−1 → LUMO] transitions while S_3 and T_5 excited states of **1b** are derived from ^{1,3}[H−2 → LUMO] transitions. The d-orbitals involved in the T_2 of **1a** and T_4 of **1b** have the same orientations as their respective S_1 excited state (see Tables S5, S6 and S9 in ESI†). The wavy blue arrows indicate internal conversion (IC) from the T_5 to T_1 excited state. F = fluorescence and P = phosphorescence.
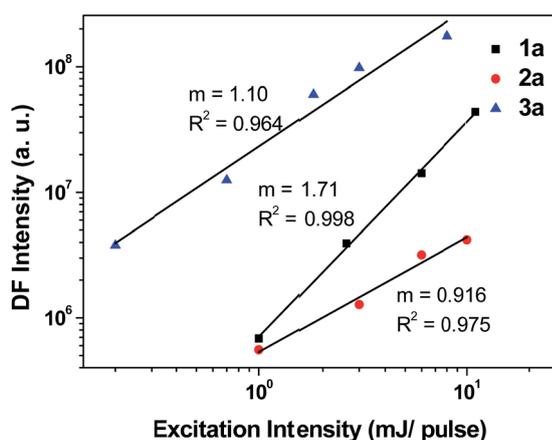

Fig. 12 Dependence of delayed fluorescence of **1a–3a** in 5×10^{-5} M degassed CH_2Cl_2 with excitation power intensity. Emission intensity measured after a time delay of 1 μs. (Laser λ_{exc} = 355 nm; 0.2–11 mJ per pulse; diameter = 8 mm, integration time: 800 μs.)

Conclusion

A series of gold complexes with different oxidation states, gold(I) complexes [LAu(C≡CR)] and gold(III) complexes [Au(C^N^C)(C≡CR)] bearing the same heterocyclic arylacetylides with narrow bandgap were synthesized and characterized. The photophysical behaviors with the gold ion in different oxidation states are strikingly different: fluorescence dominates the luminescence of the Au(I) complexes while phosphorescence takes over in the Au(III) complexes. Detailed computational studies by DFT/TDDFT have accounted for these phenomena as a result of different coordination environments inherited from the gold ion in a particular oxidation state: a linear coordination geometry for Au(I) and a square-planar coordination geometry for Au(III). This difference in

coordination geometry subtly affects the energy separation between the coupling singlet and triplet excited states, leading to smaller ΔE_{ST} of the Au(III) complexes than the Au(I) complexes and hence, larger k_{ISC} in the Au(III) complexes than the Au(I) complexes. For the complexes bearing Bodipy-functionalized acetylide ligand, they only display prompt fluorescence. Computational analyses revealed that, due to the especially narrow bandgap of Bodipy, the ΔE_{ST} is still large even in the Au(III) complex so that k_{ISC} could not compete with fluorescence radiative decay. Additionally, the mechanisms for the generation of DF in Au(I) complexes have been explored. To the best of our knowledge, this is the first report which systematically studies the effects of the metal ion oxidation state on the photophysical behaviours of transition-metal complexes.

Acknowledgements

Notes and references

1 M. Chergui, *Acc. Chem. Res.*, 2015, **48**, 801.
2 M. Montalti, A. Credi, L. Prodi and M. T. Gandolfi, *Handbook of Photochemistry*, CRC Press, USA, 2006, 3rd edn.

3 (a) A. Steffan, M. G. Tay, A. S. Batsanov, J. A. K. Howard, A. Beedy, K. Q. Vuong, X.-Z. Sun, M. W. George and T. B. Marder, *Angew. Chem., Int. Ed.*, 2010, **49**, 2349; (b) A. Steffan, R. M. Ward, M. G. Tay, R. M. Edkins, F. Seeler, M. van Leeuwen, L.-O. Palsson, A. Beeby, A. S. Batsanov, J. A. K. Howard and T. B. Marder, *Chem.–Eur. J.*, 2014, **20**, 3652; (c) A. Steffan, K. Costuas, A. Boucekkine, M.-H. Thibault, A. Beeby, A. S. Batsanov, A. Charaft-Eddin, D. Jacquemin, J.-F. Halet and T. B. Marder, *Inorg. Chem.*, 2014, **53**, 7055.

4 (a) H. Weissman, E. Shirman, T. Ben-Moshe, R. Cohen, G. Leitus, L. J. W. Shimon and B. Rybtchinski, *Inorg. Chem.*, 2007, **46**, 4790; (b) W. Y. Heng, J. Hu and J. H. K. Yip, *Organometallics*, 2007, **26**, 6760; (c) S. Lentijo, J. A. Miguel and P. Espinet, *Inorg. Chem.*, 2010, **49**, 9169; (d) V. Prusakova, C. E. McCusker and F. Castellano, *Inorg. Chem.*, 2012, **51**, 8589; (e) M.-H. Nguyen, C.-Y. Wong and J. H. K. Yip, *Organometallics*, 2013, **32**, 1620; (f) S. Lentijo, G. Aullon, J. A. Miguel and P. Espinet, *Dalton Trans.*, 2013, **42**, 6353.

5 (a) W. Lu, N. Zhu and C.-M. Che, *J. Organomet. Chem.*, 2003, **670**, 11; (b) G. S. M. Tong, P. K. Chow and C.-M. Che, *Angew. Chem., Int. Ed.*, 2010, **49**, 9206.

6 (a) H.-Y. Chao, W. Lu, Y. Li, M. C. W. Chan, C.-M. Che, K.-K. Cheung and N. Zhu, *J. Am. Chem. Soc.*, 2002, **124**, 14696; (b) W. Lu, W.-M. Kwok, C. Ma, C. T.-L. Chan, M.-X. Zhu and C.-M. Che, *J. Am. Chem. Soc.*, 2011, **133**, 14120; (c) C. Ma, C. T.-L. Chan, W.-M. Kwok and C.-M. Che, *Chem. Sci.*, 2012, **3**, 1883.

7 A. Möller, P. Bleckenwegner, U. Monkowius and F. Mohr, *J. Organomet. Chem.*, 2016, **813**, 1.

8 (a) J. Arcau, V. Andermark, E. Aguiló, A. Gandioso, A. Moro, M. Cetina, J. C. Lima, K. Rissanen, I. Ott and L. Rodríguez, *Dalton Trans.*, 2014, **43**, 4426; (b) A. J. Moro, B. Rome, E. Aguiló, J. Arcau, R. Puttreddy, K. Rissanen, J. C. Lima and L. Rodríguez, *Org. Biomol. Chem.*, 2015, **13**, 2026.

9 E. E. Langdon-Jones, D. Lloyd, A. J. Hayes, S. D. Wainwright, H. J. Mottram, S. J. Coles, P. N. Horton and S. J. A. Pope, *Inorg. Chem.*, 2015, **54**, 6606.

10 A. Meyer, C. P. Bagowski, M. Kokoschka, M. Stefanopoulou, H. Alborzinia, S. Can, D. H. Vlecken, W. S. Sheldrick, S. Wölfl and I. Ott, *Angew. Chem., Int. Ed.*, 2012, **51**, 8895.

11 E. E. Langdon-Jones and S. J. A. Pope, *Chem. Commun.*, 2014, **50**, 10343.

12 (a) C.-M. Che, H.-Y. Chao, V. M. Miskowski, Y. Li and K.-K. Cheung, *J. Am. Chem. Soc.*, 2001, **123**, 4985; (b) W. Lu, H.-F. Xiang, N. Zhu and C.-M. Che, *Organometallics*, 2002, **21**, 2343; (c) W. Lu, N. Zhu and C.-M. Che, *J. Am. Chem. Soc.*, 2003, **125**, 16081.

13 (a) V. W.-W. Yam, K. M.-C. Wong, L.-L. Hung and N. Zhu, *Angew. Chem., Int. Ed.*, 2005, **44**, 3107; (b) V. K.-M. Au, K. M.-C. Wong, D. P.-K. Tsang, M.-Y. Chan, N. Zhu and V. W.-W. Yam, *J. Am. Chem. Soc.*, 2010, **132**, 14273; (c) D.-A. Roşca, D. A. Smith and M. Bochmann, *Chem. Commun.*, 2012, **48**, 7247; (d) W.-P. To, G. S.-M. Tong, W. Lu, C. Ma, J. Liu, A. L.-F. Chow and C.-M. Che, *Angew. Chem., Int. Ed.*, 2012, **51**, 2654; (e) W.-P. To, K. T. Chan, G. S. M. Tong, C. Ma, W.-M. Kwok, X. Guan, K.-H. Low and C.-M. Che, *Angew. Chem., Int. Ed.*, 2013, **52**, 6648.

14 (a) A. L.-F. Chow, M.-H. So, W. Lu, N. Zhu and C.-M. Che, *Chem.–Asian J.*, 2011, **6**, 544; (b) J. Gil-Rubio, V. Cámara, D. Bautista and J. Vicente, *Organometallics*, 2012, **31**, 5414.

15 I. E. Pomestchenko and F. N. Castellano, *J. Phys. Chem. A*, 2004, **108**, 3485.

16 R. A. Vogt, M. A. Peay, T. G. Gray and C. E. Crespo-Hernández, *J. Phys. Chem. Lett.*, 2010, **1**, 1205.

17 F. Frei, A. Rondi, D. Espa, M. L. Mercuri, L. Pilia, A. Serpe, A. Odeh, F. V. Mourik, M. Chergui, T. Feurer, P. Deplano, A. Vlček Jr and A. Cannizzo, *Dalton Trans.*, 2014, **43**, 17666.

18 K.-C. Tang, K. L. Liu and I.-C. Chen, *Chem. Phys. Lett.*, 2004, **386**, 437.

19 (a) A. Cannizzo, F. van Mourik, W. Gawelda, G. Zgrablic, C. Bressler and M. Chergui, *Angew. Chem., Int. Ed.*, 2006, **45**, 3174; (b) W. Gawelda, A. Cannizzo, V.-T. Pham, F. van Mourik, C. Bressler and M. Chergui, *J. Am. Chem. Soc.*, 2007, **129**, 8199.

20 A. Cannizzo, A. M. Blanco-Rodríguez, A. El Nahhas, J. Šebera, S. Záliš, A. Vičcek Jr and M. Chergui, *J. Am. Chem. Soc.*, 2008, **130**, 8967.

21 (a) G. J. Hedley, A. Ruseckas and I. D. W. Samuel, *Chem. Phys. Lett.*, 2008, **450**, 292; (b) G. J. Hedley, A. Ruseckas and I. D. W. Samuel, *J. Phys. Chem. A*, 2009, **113**, 2.

22 G. Ramakrishna, T. Goodson III, J. E. Rogers-Haley, T. M. Cooper, D. G. McLean and A. Urbas, *J. Phys. Chem. C*, 2009, **113**, 1060.

23 R. A. Vogt, T. G. Gray and C. E. Crespo-Hernández, *J. Am. Chem. Soc.*, 2012, **134**, 14808.

24 O. Bräm, F. Messina, E. Baranoff, A. Cannizzo, M. K. Nazeeruddin and M. Chergui, *J. Phys. Chem. C*, 2013, **117**, 15958.

25 (a) K. Li, G. Cheng, C. Ma, X. Guan, W.-M. Kwok, Y. Chen, W. Lu and C.-M. Che, *Chem. Sci.*, 2013, **4**, 2630; (b) G. Cheng, S. C. F. Kui, W.-H. Ang, M.-Y. Ko, P.-K. Chow, C.-L. Kwong, C.-C. Kwok, C. Ma, X. Guan, K.-H. Low, S.-J. Su and C.-M. Che, *Chem. Sci.*, 2014, **5**, 4819.

26 D. N. Kozhevnikov, V. N. Kozhevnikov, M. Z. Shafikov, A. M. Prokhorov, D. W. Bruce and J. A. G. Williams, *Inorg. Chem.*, 2011, **50**, 3804.

27 Y.-M. Cheng, Y.-S. Yeh, M.-L. Ho and P.-T. Chou, *Inorg. Chem.*, 2005, **44**, 4594.

28 C.-C. Hsu, C.-C. Lin, P.-T. Chou, C.-H. Lai, C.-W. Hsu, C.-H. Lin and Y. Chi, *J. Am. Chem. Soc.*, 2012, **134**, 7715.

29 T. Hofbeck, Y. C. Lam, M. Kalbáč, S. Záliš, A. Vlček Jr and H. Yersin, *Inorg. Chem.*, 2016, **55**, 2441.

30 (a) K. Hensel and H. Bässler, *Adv. Mater. Opt. Electron.*, 1992, **1**, 179; (b) A. Hayer, H. Bässler, B. Falk and S. Schrader, *J. Phys. Chem. A*, 2002, **106**, 11045; (c) A. Köhler and H. Bässler, *Mater. Sci. Eng., R*, 2009, **66**, 71.

31 M. Aydemir, V. Jankus, F. B. Dias and A. Monkman, *Phys. Chem. Chem. Phys.*, 2014, **16**, 21543.